Lower Bound Estimates for Electrophysiological Power Dissipation in Human Gray Matter

Vikram Nathan[1], Malte Hoeltershinken[2], Eleanor Hill[1], Carsten Wolters[2], Sylvain Baillet[1,3,4]

Affiliations:
[1]Montreal Neurological Institute, McGill University, Montréal QC, Canada
[2]Institute for Biomagnetism and Biosignalanalysis, University of Münster, Münster, Germany
[3]Centre de Recherche du Centre Hospitalier de l'Université de Montréal (CRCHUM), Montréal, QC, Canada
[4]Department of Neuroscience, Université de Montréal, Montréal, QC, CA

Abstract

The human brain is popularly described as remarkably energy efficient, with its metabolic power consumption estimated at approximately 20 watts (W). Biophysical models have partitioned this power budget across distinct cellular processes, but these theoretical estimates have yet to be empirically constrained using whole-brain electrophysiological data.

Here, we used magnetoencephalography (MEG) source imaging of resting-state human brain activity to derive empirical lower-bound estimates of electrical power dissipation in cortical gray matter. We found that the total power dissipated by currents, primarily associated with post-synaptic potentials, ranges between 10^{-9} and 10^{-10} W, several orders of magnitude lower than prevailing metabolic estimates. Using finite element modeling (FEM), we observed that electrophysiological power dissipation is predominantly confined to gray matter.

Additionally, spatial variations in MEG-derived power dissipation partially correlated with regional oxygen metabolism measured by PET, yet notable discrepancies emerged across large-scale functional brain networks. These results underscore a critical divergence between electrophysiological and metabolic indices of brain energy use, and highlight the need for more integrated biophysical models to bridge this gap and better characterize the physiological underpinnings of regional brain energetics.

Introduction

The human brain processes information with remarkable power efficiency, requiring less power than a typical laptop computer (approximately 20 W; Balasubramanian, 2021). This estimate of total power demand is primarily derived from stoichiometric calculations of oxygen and glucose consumption measured by positron emission tomography (PET) and adenosine triphosphate (ATP) turnover determined by ^{31}P magnetic resonance spectroscopy imaging (Clarke & Sokoloff, 1999; Zhu et al., 2012). Despite this general understanding, precisely quantifying the energetic costs of distinct neuronal processes remains challenging.

Mathematical "power budget" models based on electrophysiological properties of neurons have offered theoretical partitions of this consumption. Such models translate measured ionic fluxes into power expenditures associated with distinct neural processes, for example, differentiating between white versus gray matter signaling, and action potential conduction versus passive membrane properties (Attwell & Laughlin, 2001; Lennie, 2003). Levy & Calvert (2021) further partitioned gray matter activity into "communication" and "computation," showing computation to be ~35 times more efficient and contributing ~0.1 W of the brain's overall power. However, this theoretical prediction has yet to be empirically validated with whole-brain electrophysiological measures in humans.

Previous work indicates that postsynaptic potentials constitute a substantial portion of gray matter's energetic demand, largely due to sodium and potassium currents associated with synaptic transmission (Alle et al., 2009). At the whole-brain scale, electrophysiological and hemodynamic recordings in non-human primates have demonstrated that local field potentials (LFPs), primarily reflecting postsynaptic potentials, predict resting-state hemodynamic fluctuations better than action potentials (Logothetis, 2008). Yet, the precise energetic cost of generating large-scale synchronized postsynaptic activity across the human cortex remains unknown.

To address this critical gap, we developed a data-driven approach leveraging the high temporal resolution and cortical specificity of magnetoencephalography (MEG; Baillet, 2017). Specifically, we sought to empirically estimate the electrical power dissipation directly associated with cortical current fluctuations in task-free, resting behavior. By constraining our source mapping to primary current dipoles at vertices of the cortical mesh, we derived estimates of power dissipation, establishing an empirical lower bound for the energetic costs of intrinsic cortical activity.

Methods

MEG and MRI Data Acquisition

Resting-state MEG data were acquired from five healthy adult participants (age range: 21-30 years, 2 females) in five-minute eyes-open resting sessions on a CTF 275-channel MEG system (CTF MEG International Services LP, Coquitlam, Canada) at 2400 Hz sampling rate. Data were recorded with an anti-aliasing low-pass filter below 600 Hz. Individual head shape, captured at approximately 100 scalp locations, and fiducial points (nasion, left and right preauricular points) were digitized with a Polhemus Fastrak system using *Brainstorm* (Tadel et al., 2011) and co-registered to T1-weighted MRI volumes processed in *FreeSurfer* 5.3 for tissue segmentation and cortical surface mesh triangulation (Fischl et al., 2012).

FEM Mesh Creation and Forward Modelling

Three-layer finite element method (FEM) meshes were generated for each participant, with layers corresponding to: Brain (combining gray matter, white matter, and CSF), Skull (combining compact and spongiform bone), and Scalp tissues.

We verified that three-layer meshes produced power dissipation estimates comparable to five-layer models (Supplementary Figure 1). Surfaces for the head, outer skull, and inner skull were generated from each participant's T1 MRI using Brainstorm's boundary element model implementation. Iso2Mesh (Tran et al., 2020) was then used to generate the FEM mesh, with the "MergeMesh" option selected to tessellate internal cavities.

Default conductivity values were set to 0.33 S/m for brain and scalp, and 0.0042 S/m for skull (Oostenveld et al., 2011). For four of five participants, this procedure successfully produced three-layer meshes (mean: ~51,700 vertices and ~276,000 elements; Figure 3C). FEM modeling enabled estimation of secondary currents across tissue layers, complementing primary dipole-based estimates. All further FEM analyses excluded the one subject for whom modeling failed.

MEG Source Mapping

Preprocessing followed good-practice guidelines (Gross et al, 2017), including artifact (e.g., cardiac and ocular) removals by signal-space projection (SSP) available in *Brainstorm*. Forward modeling was performed with the DUNEuro module in *Brainstorm* (Schrader et al., 2021; Medani et al., 2021; Tadel et al., 2011). Environmental noise covariance was estimated from two-minute empty-room recordings acquired immediately prior to each MEG session.

Source reconstruction was performed using minimum norm estimation (MNE) implemented in *Brainstorm*, with default hyperparameter settings (Tadel et al., 2011). Source activity was

constrained to the surface halfway between the gray matter/cerebrospinal fluid and gray matter/white matter boundary, with 15,002 dipoles per participant, with unconstrained orientation. This framework yielded spatially resolved time series of cortical current amplitudes.

Validation with Physical Phantoms

To validate current recovery, MEG data were recorded from two calibration phantoms: CTF phantom (single dipole in a conducting sphere), and Elekta phantom (32 open-air dipoles arranged under a hemispherical surface; Figure 2A).

For the CTF phantom, oscillatory currents were set at 7 Hz and 23 Hz with amplitudes of 1800 nA·m and 180 nA·m, respectively, over 10-second recordings. For the Elekta phantom, oscillatory currents at 1000 Hz (resampled to 100 Hz) were set at 20, 200, and 2000 nA·m over 8-second epochs.

The same source mapping pipeline as for human data was applied. Data were segmented into epochs corresponding to individual oscillatory cycles (140 ms for 7 and 23 Hz; 400 ms for 1000 Hz). We averaged the MEG data across all epochs to reduce noise before our MNE source reconstruction. We identified the time points of peak current emission and calculated the MNE-reconstructed amplitudes at each of these peaks. Total reconstructed current strength was computed by summing across all dipole sources.

This epoching and averaging procedure yielded three "peak" current estimates for the 1800 nA·m current dipole and seven peaks for the 180 nA·m dipole from the CTF phantom. There was only one peak (60 ms) for the Elekta phantom, but the source could be localized separately at this peak for each of the 32 dipoles. In both cases, reconstructed currents closely approximated ground-truth values, supporting the robustness of our approach for quantifying absolute current magnitudes and subsequent power dissipation.

Cortical Columnar vs. FEM-Derived Power

(i) Primary Cortical Columnar Power

We estimated cortical power dissipation using Ohm's law, with current amplitudes (I) derived from MEG source reconstructions and resistance (R) from co-registered structural MRI data. Neural impedance was assumed to be purely resistive, neglecting capacitive and inductive components (Baillet et al., 2001).

The downsampled version of the Freesurfer surface mesh (15,002 vertices) was used to define vertices on the cortex, as well as the support area (A) attached to each vertex. CAT12 was used to calculate cortical thickness (L) at each vertex due to the increased efficiency of its implementation in Brainstorm

Resistance (R) was then calculated as:

$$R = \rho L/A \tag{1}$$

where ρ is cortical resistivity (3.5 Ω.m; Abboud et al., 2021); L is cortical thickness (taken as dipole length) and A is surface area, defined as one-third of the area of all the neighboring mesh triangles (Hillebrand & Barnes, 2002).

Power dissipation (P) at each cortical vertex was then defined as:

$$P = I^2 R \tag{2}$$

Substituting $I = I_{dip}/L$, with I_{dip} as the dipole current estimated from MEG:

$$P = \rho I_{dip}^2/(L \cdot A) \tag{3}$$

Vertex-wise estimates at each dipole were termed "primary dipole P," and their sum across all vertices was termed "total primary P" (see Figure 1 for workflow).

(ii) Secondary Current Power (FEM)

Secondary volume currents in head tissues (gray matter, white matter, skull, scalp) were estimated using FEM-derived electric fields (E). After computing the electric field E due to neural activity, the associated secondary currents density (j^S) was defined as

$$j^S = \sigma \cdot E,$$

where σ denotes tissue conductivity (Hämäläinen et al., 1993). The corresponding power dissipation was then computed as:

$$P = \int_V < E, j^S > dV = \int_V < E, \sigma E > dV = \int_V < \sigma |E|^2 dV \tag{4}$$

where ⟨E,j⟩ denotes the inner product (Griffiths, 2023, Chapter 8.1.2).

FEM simulations were performed using the Python interface of the DUNEuro toolbox (Schrader et al, 2021; Hölteshinken et al., 2025). A continuous Galerkin approach with piecewise affine trial and test functions was applied, with partial integration used to handle dipole singularities. Due to computational demands, secondary fields were estimated from the root-mean-square primary dipole over a 120-second resting-state segment, rather than at each time point.

Neural activity was modeled as a linear combination of k current dipoles. For each dipole at position x_i with moment M_i, the FEM solver generated a corresponding field vector E_i. By linearity of the governing equations, the total field was:

$$E = \sum_{i=1}^{k} E_i.$$

We then computed two metrics:

Total secondary power:

$$P^{S}_{total} := \int_{V} < \sum_{i=1}^{k} E_{i}, \sigma \cdot \sum_{i=1}^{k} E_{i} > dV \tag{5}$$

Secondary dipole power:

$$P^{S}_{dipole} := \sum_{i=1}^{k} \int_{V} < E_{i}, \sigma \cdot E_{i} > dV \tag{6}$$

Finally, note that in the special case of a current *I* passing through a resistor *R*, the general FEM formulation reduces to the Ohmic definition in equation (2). Thus, his framework generalizes the primary columnar model to more complex, anisotropic conductors.

Dendritic vs. Gray Matter-Derived Resistances

Our "primary dipole P" framework estimates electrical resistance within each cortical column by assuming uniform gray-matter resistivity, scaled by cortical thickness and surface area. However, because cortical tissue also includes non-neuronal components, we derived a complementary estimate of resistance attributable specifically to ensembles of parallel apical dendrites. This served to validate the gray matter-based resistance model with a more biophysically grounded neuronal model.

To approximate the resistance of Layer 5 pyramidal neurons (the cell population most often considered the principal generator of MEG signals), we used established values from Kasevich and LaBerge, 2011. for dendritic resistivity (29.7 ohm-cm), length (1200 µm), and cross-sectional area, assuming a circular cross-section with a 5 µm diameter. Single-neuron resistance was calculated from Equation 1, yielding $R_{neuron}=1.816*10^{7}\ \Omega$.

We then estimated the number of apical dendrites contributing to the signal of each cortical column using the following procedure:

1. Parcel assignment: Each cortical vertex was assigned to a Desikan-Killiany-Tourville (DKT) atlas parcel based on *FreeSurfer 5.3* parcellations (Fischl et al., 2012).
2. Neuronal fraction: The neuronal volume fraction (p_{neur}) for each parcel was extracted from cell-type deconvolution of the Allen Human Brain Atlas (Pak et al., 2023).
3. Density scaling: p_{neur} was multiplied by published neuron density estimates (neurons/mm^2) for gross anatomical regions (e.g., frontal, temporal, occipital; see Klein and Tourville (2012)), derived from DAP staining (Ribeiro et al., 2013).

4. Column scaling: This density was multiplied by the support area (A) in mm^2 at each vertex to yield the total number of neurons (N) per cortical column.

Assuming apical dendrites behave as resistors in parallel, the total effective resistance was given by:

$$R_{total} = R_{neuron}/N \tag{7}$$

This model was applied across the cortical surface in a representative individual and compared to gray matter-based resistance values. We found a strong correlation between the two maps (Spearman r = 0.79). Mean dendritic resistance was estimated at 178 Ω (range: 17.8–6652.6 Ω), compared to a mean gray matter columnar resistance of 714 Ω (range: 41.2–13,736 Ω).

This convergence supports the robustness of our resistance modeling framework and its suitability for estimating local power dissipation in cortical gray matter.

Results

Initial MEG-Derived Cortical Power Estimate

We first computed the mean cortical power dissipation over a five-minute resting-state MEG recording in n = 4 individuals from the OMEGA cohort (Niso et al., 2019). Across participants, mean whole-brain power dissipation was 6.8×10^{-9} W, with individual values ranging from 3.5×10^{-9} W to 8.7×10^{-9} W. These values reflect the combination of cortical currents, thickness, and resistivity used in our modeling (Figure 1B).

These estimates are several orders of magnitude lower than the ~0.1 W predicted by Levy and Calvert (2021). To test the robustness of this discrepancy, we performed three independent validations: (1) testing current recovery with physical phantoms, (2) validating resistance estimates with dendritic modeling, and (3) comparing spatial patterns of MEG-derived power dissipation with PET-based and gene expression-based cortical metabolic maps.

Importantly, these analyses were performed on a small sample size (n = 4), which we acknowledge as a limitation.

Validation of Current Estimates and Resistive Modeling

To determine whether underestimated source currents might explain the low power values, we evaluated the performance of MNE-based source reconstruction using MEG recordings from physical phantoms with known current dipole amplitudes. For the CTF phantom emitting a 1800 nA·m current dipole, MEG source estimates recovered 1575 nA.m, or 87.5% of the ground truth

amplitude. For the Elekta phantom, across 32 dipoles emitting 200 nA.m, the average reconstructed amplitude was 144.65 nA.m, or 70% of the true value (Figure 2B/C).

Even in the worst case, reconstruction errors remained within one order of magnitude, suggesting that inaccuracies in current estimation cannot account for the observed low levels of power dissipation.

To independently assess resistance estimates, we implemented the dendritic-based resistance model described above. In a representative individual, we observed a strong correlation (Spearman $r = 0.79$) between gray matter columnar resistance and dendritic resistance estimates. The dendritic model tended to yield lower resistances on average (mean 162.5 Ω) compared to the gray matter-based model (mean 714.4 Ω), but both maps exhibited similar spatial patterns (Figure 2D). This supports the robustness of our assumptions.

Although both current and resistance estimates were independently validated, our modeling is based on a simplified Ohmic circuit framework and does not account for capacitive or other dynamic elements that may contribute to actual power dissipation in neural tissue.

Increasing Spatial Resolution with Secondary Currents in FEM Mesh Does Not Increase Power Estimates

Our initial calculations estimated power dissipation at cortical surface vertices on the FEM-derived mesh, but were limited to currents within gray matter directly beneath each vertex. To extend this approach, we used the full FEM mesh, representing the entire head volume as a conductive medium composed of discrete elements, each assigned a conductivity based on tissue type (Figure 3C). This method allowed us to account for secondary currents induced by primary dipoles as they are driven throughout the head volume.

We found that total *secondary-P* was only 28–32% of the magnitude of total *primary-P*, indicating that the original estimates were not substantially underestimated (Figure 3B). Moreover, 92% of total secondary power dissipation localized to gray matter (Supplementary Figure 2), confirming our assumption that gray matter is the primary site of MEG-visible electrical dissipation. While secondary dipole P was moderately correlated with primary dipole P, its spatial distributions differed (Figure 3D), highlighting the added spatial specificity provided by FEM.

Together, these findings demonstrate that even with refined head modeling, MEG-derived power dissipation estimates remain well below theoretical metabolic predictions. This suggests that the discrepancy reflects deeper physiological differences between electrical and metabolic measures of brain activity, rather than methodological artifacts.

Power Correlations with Whole-Cortex and Within-Network Metabolism

After validating the magnitude and spatial specificity of our MEG-derived power dissipation estimates, we investigated their relationship with cortical metabolism measured by PET. "Primary dipole P" estimates were parcellated into the Schaefer-600 atlas and compared against publicly available PET datasets (Vaishnavi et al., 2010), accessed through the *neuromaps* toolbox (Markello et al., 2022). In parallel, we compared MEG-derived maps to indices of metabolic processes derived from whole-brain microarray gene expression in six postmortem subjects from the Allen Human Brain Atlas (Pourmajidian et al., 2025). For each of 22 metabolic processes, spatial maps were generated by averaging the expression of genes within the corresponding Gene Ontology term.

Across the whole cortex, we observed a significant negative correlation between MEG-derived power dissipation and PET-derived oxygen metabolism (Spearman r = -0.21, p=0.000325), outperforming the correlation between the current dipole and oxygen metabolism (Spearman r = -0.15). No significant correlation was found between power or current glucose metabolism (r = -0.025; r=-0.01, p > 0.5) (Figure 4A).

Network-level analyses revealed stronger associations (Figure 4B). In the ventral attention network, MEG-derived power dissipation showed a positive correlation with glucose metabolism (r = 0.23, p=0.047), outperforming the correlation obtained with average primary current dipole amplitudes (r = 0.21, p = 0.071).

In the default mode network (DMN), MEG-derived power dissipation also provided stronger predictive value than dipole amplitudes alone when predicting glucose and oxygen metabolism. In particular, the strongest observed correlation between PET metabolism and MEG across all networks was seen between MEG-derived power and oxygen metabolism in the default mode network (r=-0.44, p=$2.13*10^{-7}$), outperforming the primary current dipole correlation (r=-0.41, p=$1.77*10^{-6}$). Nonetheless, none of the other observed correlations in Figure 4B exceed the Bonferroni threshold, and the current dipoles often outperform the power at predicting metabolism, indicating that our power metric is not a comprehensive model of brain metabolism.

Across the 22 gene expression-derived metabolic processes, ketone body utilization and ketone metabolism displayed the highest absolute whole-brain correlations with MEG-derived power (r=0.22 and 0.21, respectively), slightly outperforming correlations with current dipole amplitudes (r=0.18 and r=0.16; Figure 5A; Supplementary Table 1). However, within networks, MEG-derived power was less correlated with ketone utilization and metabolism than dipole amplitudes. For example, in the default mode network, ketone body metabolism correlated more strongly with dipole amplitudes (r = 0.44, p=$1.74*10^{-7}$) than with power dissipation (r = 0.38, p = $9.02*10^{-6}$). Additionally, the strongest observed correlation in this dataset was between the spatial map of pyruvate carboxylase (pc) and the primary current dipole (r=-0.29, p=$8.01*10^{-13}$), a correlation that was unable to be captured by our power metric (r=-0.14, p=$4.62*10^{-4}$).

Taken together, these results suggest that MEG-derived power dissipation and metabolic measures are not uniformly aligned across the cortex, but nonetheless show meaningful regional correspondence in functionally defined networks. Notably, our power dissipation metric correlates significantly with PET-derived oxygen metabolism and gene-derived ketone metabolism within the default mode network, though with limited improvements over the current dipoles. This supports the potential of MEG-derived power as a complementary index of local cortical energetics, albeit one that reflects a different physiological substrate than PET or transcriptomic proxies.

Discussion

Discrepancy Between MEG-Derived and Metabolic Power Estimates

Our estimates of cortical power dissipation from resting-state MEG recordings were several orders of magnitude lower than canonical values reported for brain metabolism (Clarke & Sokoloff, 1999; Zhu et al., 2012; Balasubramanian, 2021) and the ~0.1 W predicted for cortical computation (Levy & Calvert, 2021). Even after validation with phantoms, dendritic resistance modeling, and FEM-based refinements, MEG-derived values remained consistently low. This indicates that the discrepancy is unlikely to arise from methodological artifacts alone.

Methodological Considerations

Our approach models cortical columns using an Ohmic framework, which assumes purely resistive impedances (Baillet et al., 2001). This simplification excludes capacitive and nonlinear contributions known to exist in neuronal membranes (Gentet et al., 2000). Furthermore, each cortical column was treated independently, neglecting recurrent local connectivity and frequency-dependent impedance effects. These simplifications likely result in an underestimation of the true electrical energy cost, and thus our estimates should be interpreted as a lower bound.

Physiological Distinctions Between Electrophysiological and Metabolic Measures

Beyond modeling assumptions, fundamental physiological differences explain why MEG-derived power dissipation diverges from metabolic estimates. MEG primarily detects large-scale, synchronous cortical currents in superficial layers (Baillet, 2017; Baillet, Mosher, & Leahy, 2001). In contrast, the majority of metabolic consumption arises from processes invisible to MEG, including synaptic vesicle cycling, neurotransmitter reuptake, and the maintenance of resting membrane potentials (Alle et al., 2009; Castrillón et al., 2023). Additionally, MEG captures neural dynamics at the millisecond timescale, whereas PET provides time-averaged measures of biochemical energy use over tens of minutes (Clarke & Sokoloff, 1999; Vaishnavi et al., 2010). These differences in spatial and temporal sensitivity contribute to the observed mismatch in magnitude.

Regional Correspondences With PET and Gene Expression

Despite the overall discrepancy, meaningful regional associations emerged. MEG-derived power dissipation correlated positively with glucose metabolism in the ventral attention network and negatively with both glucose and oxygen metabolism in the default mode network. These correlations were stronger than those obtained using dipole amplitudes alone, suggesting that modeling power provides a more physiologically relevant index of local energetics.

Our transcriptomic analyses further extended these findings. Whole-brain comparisons revealed modest correlations between MEG-derived power and gene-expression proxies of ketone metabolism and utilization (Pourmajidian et al., 2025). These associations slightly outperformed dipole-based measures at the whole-cortex level but varied across networks. For example, in the dorsal attention and default mode networks, ketone metabolism aligned more strongly with dipole amplitudes than with power dissipation. This variability underscores that electrophysiological and biochemical measures capture distinct but partially overlapping facets of cortical energetics.

Implications and Future Directions

Taken together, our results indicate that MEG-derived power dissipation represents a biologically meaningful *lower bound* on the energetic cost of synchronized cortical activity. While incomplete in absolute terms, this measure offers comparative value, for example, in studies of aging, disease, or pharmacological modulation of cortical efficiency.

Future work should focus on three areas: 1) Model refinement: Incorporating capacitive and nonlinear elements into MEG-informed models (Gentet et al., 2000); 2) Multimodal integration: Employing simultaneous MEG–PET studies to more directly reconcile electrophysiological and metabolic measures and 3) Population studies: Expanding sample sizes and extending analyses to patient cohorts to evaluate how MEG–metabolism correspondences vary across lifespan and disease.

By bridging electrophysiological and metabolic perspectives, our framework contributes to a multiscale understanding of brain energetics and provides a foundation for future integrative models.

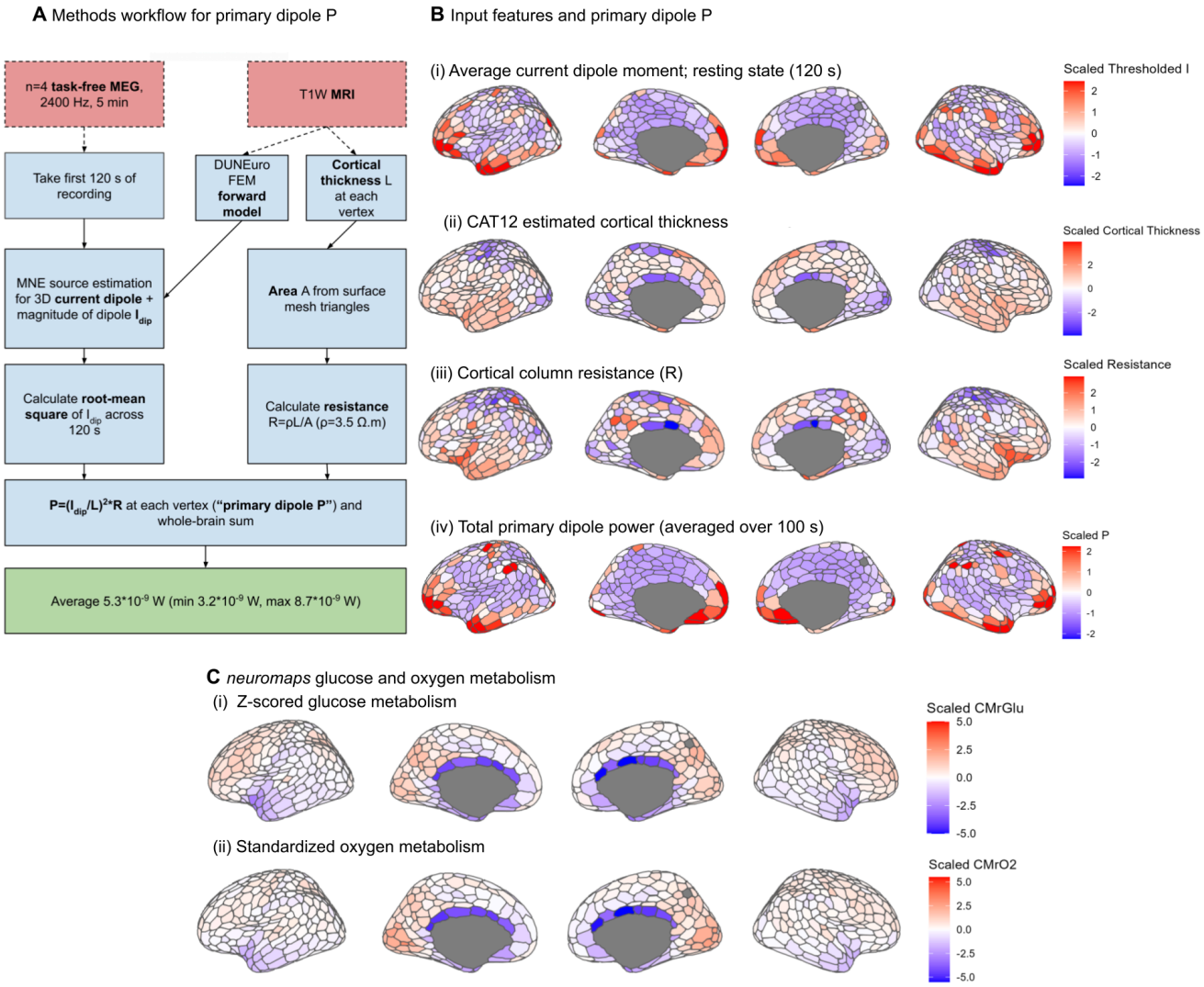

Figure 1: Methods workflow (Fig. 1A) and input features (Fig. 1B) used to calculate cortical power consumption at primary current dipoles (primary dipole P). All visualizations in 1B and 1C are shown using the Schaefer 600 parcellation using *ggseg*. Figure 1B denotes the input features (MNE current dipole, CAT12 cortical thickness, cortical column resistance) used to calculate the final map of total primary dipole power across n=4 OMEGA individuals. Figure 1C shows maps from the neuromaps toolbox representing glucose and oxygen metabolism from n=33 individuals, originally published in Vaishnavi et al., 2010. All outliers, defined as beyond 1.5 times the interquartile range from the median of each map, were replaced with the largest or smallest non-outlier value. All values were then z-scored for visual comparison. Note that the region "7Networks_Default_pCunPCC_14" is missing due to issues parcellating the primary current dipole in *Brainstorm*.

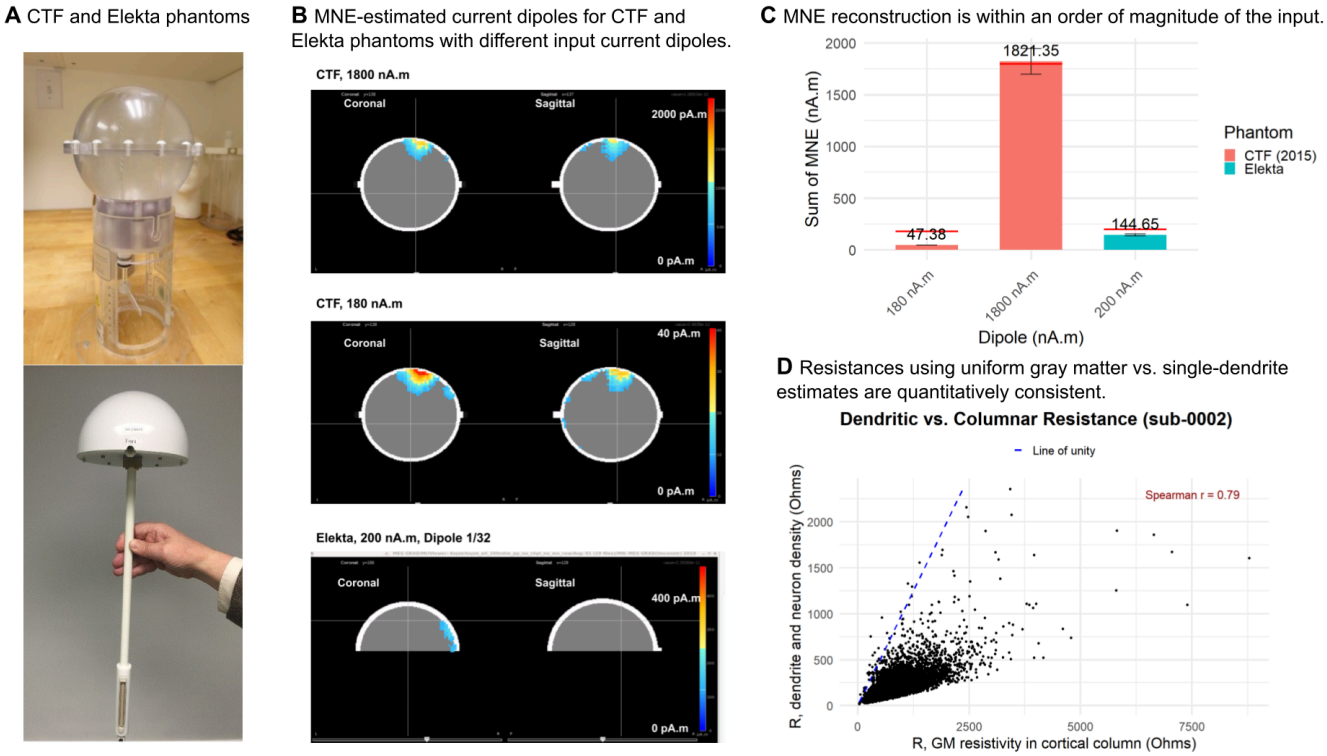

Figure 2: Confirmations of current and resistance estimates. Fig. 2A shows the CTF (upper) and Elekta (lower) phantoms used to emit known current strengths. Fig 2B. shows representative maps of minimum-norm estimation (MNE) reconstructions of the emitted dipoles, which were summed up to produce the values in Figure 2C. Fig. 2C shows the mean and standard deviation of the total MNE reconstruction of the averaged phantom signal at points of "peak" amplitude (see Validation with Physical Phantoms). Fig. 2D confirms the robustness of our initial resistance estimates by comparing them against an alternative formulation with cell-derived resistances and estimated cell counts across the brain (see Dendritic vs. Gray Matter Derived Resistances). Note that the top-right outlier value was removed from this plot for a more balanced visualization.

A Methods workflow

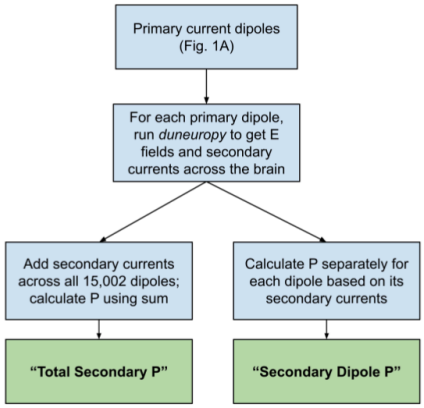

B Total secondary P is within the same order of magnitude but smaller than primary P.

Subject	Primary Dipole P (nW)	Total Sec. P (nW)	Summed Sec. Dipole P (nW)	Sec. and Pri. Dipole P Correlation (Pearson r)	% Total Sec. P vs. Pri. Dip. P
sub-0002	8.66	2.36	0.85	0.29	27.3
sub-0004	7.64	1.78	0.58	0.11	23.3
sub-0006	3.51	0.935	0.32	0.36	26.6
sub-0007	7.08	1.82	0.59	0.26	25.7

C Representative three-layer FEM mesh

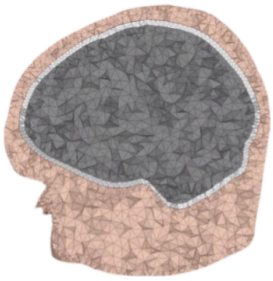

D FEM primary dipole P and secondary dipole P show spatial differences.

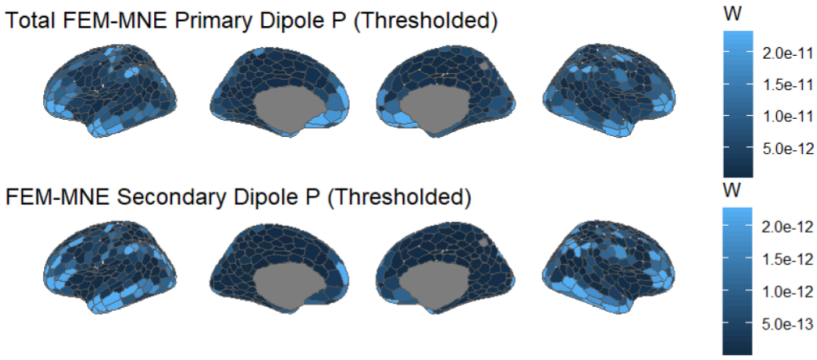

Figure 3: Derivations of FEM-derived secondary power consumption. Fig. 3A shows the methods workflow for deriving secondary dipole P and total secondary P, which are shown for each of our n=4 individuals in 3B. Fig. 3B also shows the correlation between the primary dipole P and summed secondary dipole P. Fig. 3C shows a representative FEM mesh used to derive the power estimations. Fig. 3D uses *ggseg* to visualize the spatial differences in the primary and secondary dipole P averaged across all individuals.

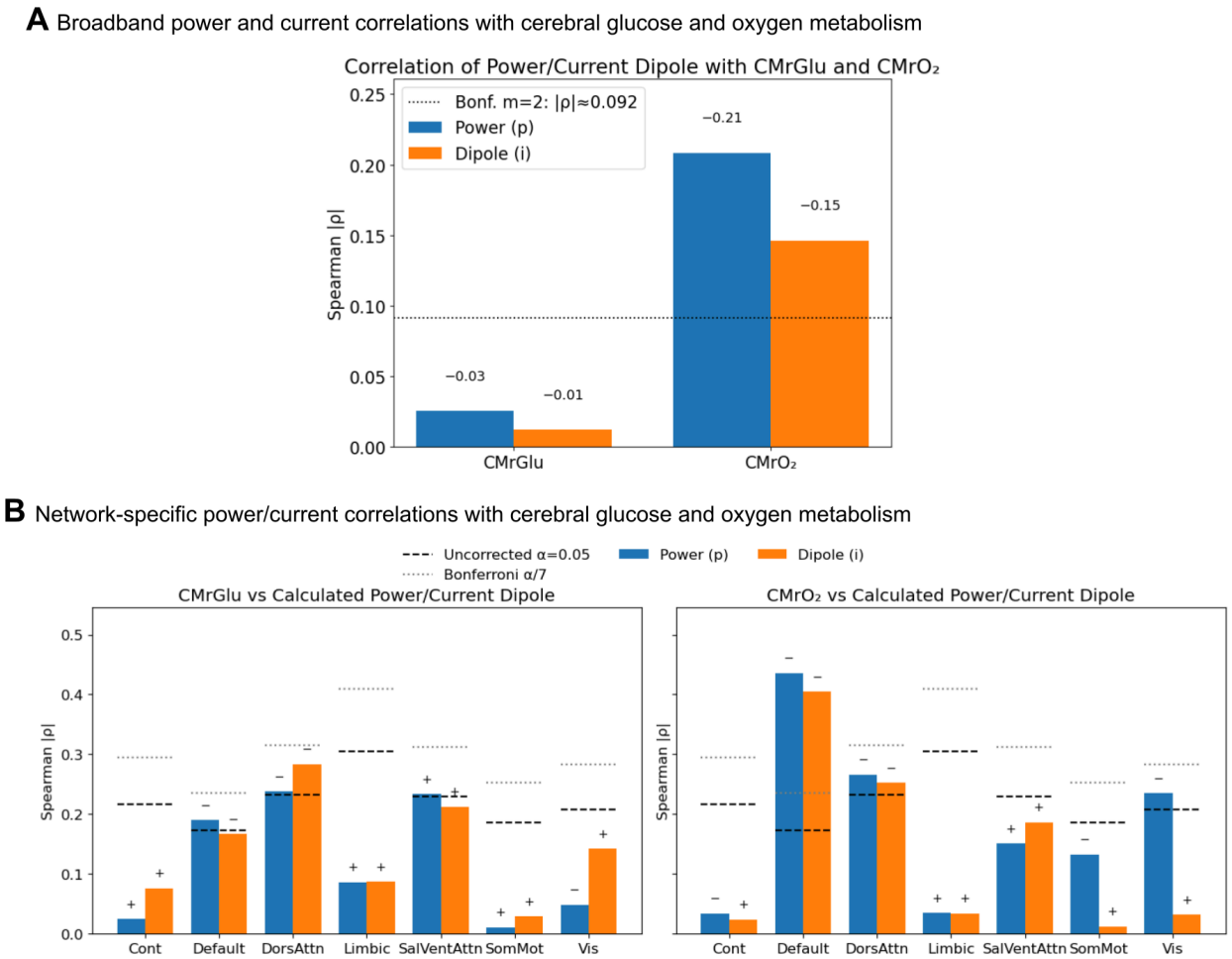

Figure 4: Correlations between the parcellated power dissipation and PET-derived metabolism maps in different functional networks. Figure 4A correlates primary dipole P and the values of the primary current dipoles against glucose and oxygen metabolism in all n=600 Schaefer parcels. Figure 4B disentangles the correlation between power dissipation and metabolism within specific functional networks, defined by Yeo et al. 2011. Note that each network has a different Spearman correlation threshold for "significance" before and after Bonferroni correction due to the different number of parcels within each network. Abbreviations: CMrGlu: cerebral metabolic rate of glucose (glucose metabolism); $CMrO_2$: cerebral metabolic rate of oxygen (oxygen metabolism).

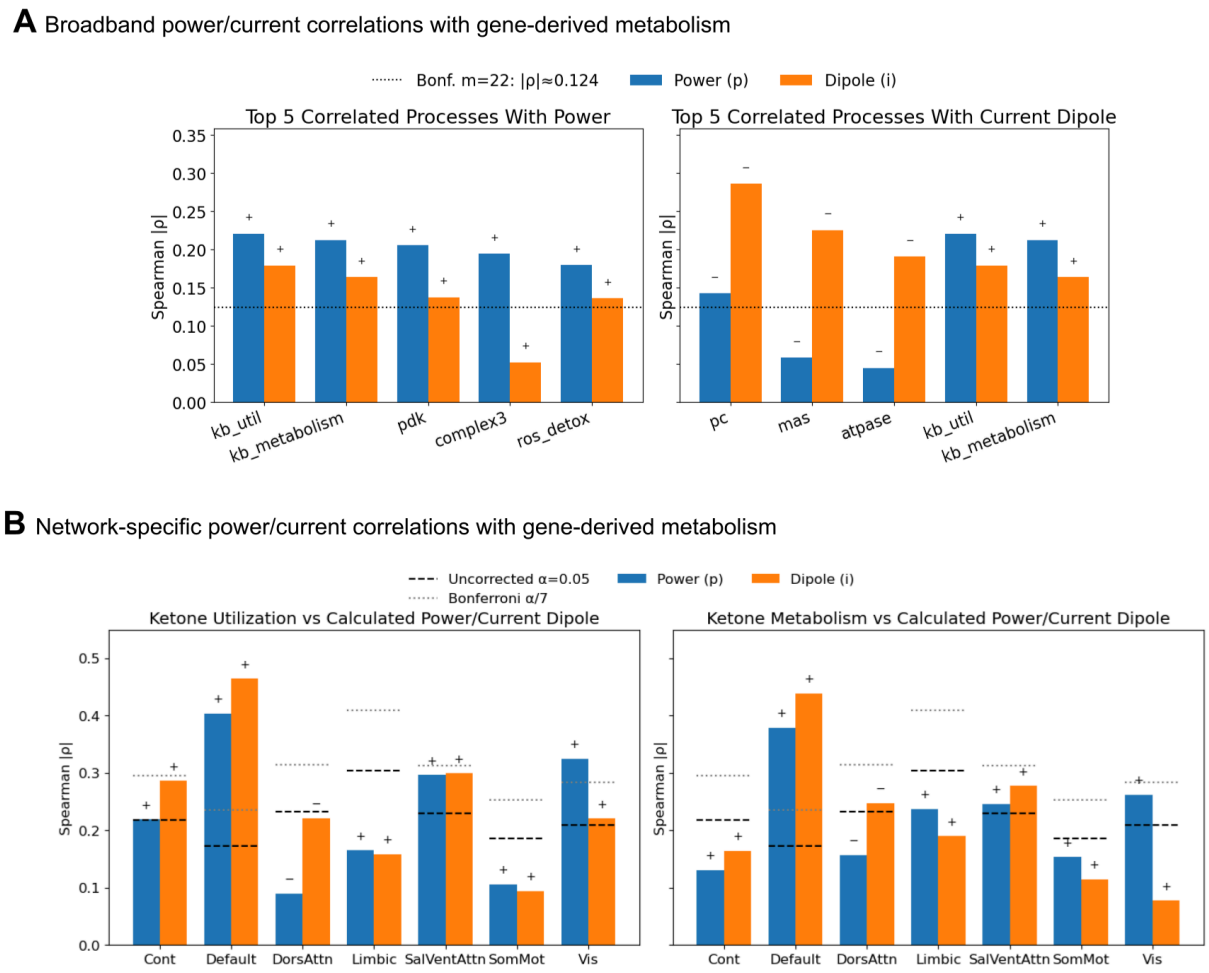

Figure 5: Correlations between the parcellated power dissipation and gene set-derived metabolism maps in different functional networks (see Pourmajidian et al., 2025). Figure 5A correlates primary dipole P and the values of the primary current dipoles against the top five out of the 22 gene set-derived metabolic maps. Figure 5B disentangles the relationship between power dissipation, current dipole and ketone metabolism within the Yeo networks. Abbreviations: kb_util: ketone body utilization, kb_metabolism: ketone body metabolism; pdk: pyruvate dehydrogenase kinase; complex3: Complex III of the electron transport chain; ros_detox: detoxification of reactive oxygen species; pc: pyruvate carboxylase; mas: malate-aspartate shuttle; atpase: sodium/potassium ATPase pump.

Acknowledgements

The Elekta phantom data was provided by Ken Taylor and John Mosher (Epilepsy Center, Cleveland Clinic Neurological Institute, Cleveland, OH USA). The CTF phantom data was provided by Elizabeth Bock, Francois Tadel and Sylvain Baillet (MEG Lab, McConnell Brain Imaging Center, Montreal Neurological Institute, McGill University, Canada). We would like to thank Moohebat Pourmajidian for her input on extracting and processing the gene-set derived metabolism maps.

Code availability:

Code for all analyses is available at https://github.com/vik16nathan/meg_power.

Bibliography

Abboud, T., Hahn, G., Just, A., et al. (2021). An insight into electrical resistivity of white matter and brain tumors. *Brain Stimulation, 14*(8), 1307–1316. https://doi.org/10.1016/j.brs.2021.08.023

Alle, H., Roth, A., & Geiger, J. R. P. (2009). Energy-efficient action potentials in hippocampal mossy fibers. *Science, 325*(5946), 1405–1408. https://doi.org/10.1126/science.1174331

Attwell, D., & Laughlin, S. B. (2001). An energy budget for signaling in the grey matter of the brain. *Journal of Cerebral Blood Flow & Metabolism, 21*(10), 1133–1145. https://doi.org/10.1097/00004647-200110000-00001

Baillet, S., Mosher, J. C., & Leahy, R. M. (2001). Electromagnetic brain mapping. *IEEE Signal Processing Magazine, 18*(6), 14–30. https://doi.org/10.1109/79.962275

Baillet, S. (2017). Magnetoencephalography for brain electrophysiology and imaging. *Nature Neuroscience, 20*(3), 327–339. https://doi.org/10.1038/nn.4504

Balasubramanian, V. (2021). Brain power. *Proceedings of the National Academy of Sciences, 118*(21), e2107022118. https://doi.org/10.1073/pnas.2107022118

Castrillón, G., Epp, S., Bose, A., et al. (2023). An energy costly architecture of neuromodulators for human brain evolution and cognition. *bioRxiv*. https://doi.org/10.1101/2023.04.25.538209

Clarke, D. D., & Sokoloff, L. (1999). Circulation and energy metabolism of the brain. In G. J. Siegel et al. (Eds.), *Basic Neurochemistry: Molecular, Cellular and Medical Aspects* (6th ed., pp. 637–669). Lippincott Williams & Wilkins.

Fischl, B. (2012). FreeSurfer. *NeuroImage, 62*(2), 774–781. https://doi.org/10.1016/j.neuroimage.2012.01.021

Gaser, C., Dahnke, R., Thompson, P. M., Kurth, F., & Luders, E. (2022). CAT – A computational anatomy toolbox for the analysis of structural MRI data. *bioRxiv*. https://doi.org/10.1101/2022.06.11.495736

Gentet, L. J., Stuart, G. J., & Clements, J. D. (2000). Direct measurement of specific membrane capacitance in neurons. *Biophysical Journal, 79*(1), 314–320. https://doi.org/10.1016/S0006-3495(00)76293-X

Griffiths, D. J. (2023). *Introduction to Electrodynamics* (5th ed.). Cambridge University Press.

Hämäläinen, M. S., Hari, R., Ilmoniemi, R. J., Knuutila, J., & Lounasmaa, O. V. (1993). Magnetoencephalography—theory, instrumentation, and applications to noninvasive studies of

the working human brain. *Reviews of Modern Physics, 65*(2), 413–497. https://doi.org/10.1103/RevModPhys.65.413

Holtershinken, M. B., Lange, P., Erdbrügger, T., et al. (2025). The local subtraction approach for EEG and MEG forward modeling. *SIAM Journal on Scientific Computing, 47*(1), B160–B189. https://doi.org/10.1137/21M1463855

Hillebrand, A., & Barnes, G. R. (2002). A quantitative assessment of the sensitivity of whole-head MEG to activity in the adult human cortex. *NeuroImage, 16*(3 Pt 1), 638–650. https://doi.org/10.1006/nimg.2002.1102

Kasevich, R. S., & LaBerge, D. (2011). Theory of electric resonance in the neocortical apical dendrite. *PLoS ONE, 6*(8), e23412. https://doi.org/10.1371/journal.pone.0023412

Klein, A., & Tourville, J. (2012). 101 labeled brain images and a consistent human cortical labeling protocol. *Frontiers in Neuroscience, 6*, 171. https://doi.org/10.3389/fnins.2012.00171

Lennie, P. (2003). The cost of cortical computation. *Current Biology, 13*(6), 493–497. https://doi.org/10.1016/S0960-9822(03)00135-0

Levy, W. B., & Calvert, V. G. (2021). Communication consumes 35 times more energy than computation in the human cortex, but both costs are needed to predict synapse number. *Proceedings of the National Academy of Sciences, 118*(13), e2008173118. https://doi.org/10.1073/pnas.2008173118

Logothetis, N. K. (2008). What we can do and what we cannot do with fMRI. *Nature, 453*(7197), 869–878. https://doi.org/10.1038/nature06976

Markello, R. D., Hansen, J. Y., Liu, Z.-Q., et al. (2022). neuromaps: structural and functional interpretation of brain maps. *Nature Methods, 19*(12), 1472–1479. https://doi.org/10.1038/s41592-022-01625-w

Medani, T., Garcia-Prieto, J., Tadel, F., et al. (2023). Brainstorm-DUNEuro: An integrated and user-friendly finite element method for modeling electromagnetic brain activity. *NeuroImage, 267*, 119851. https://doi.org/10.1016/j.neuroimage.2023.119851

Niso, G., Tadel, F., Bock, E., Cousineau, M., Santos, A., & Baillet, S. (2019). Brainstorm pipeline analysis of resting-state data from the Open MEG Archive. *Frontiers in Neuroscience, 13*, 284. https://doi.org/10.3389/fnins.2019.00284

Oostenveld, R., Fries, P., Maris, E., & Schoffelen, J.-M. (2011). FieldTrip: Open source software for advanced analysis of MEG, EEG, and invasive electrophysiological data. *Computational Intelligence and Neuroscience, 2011*, 156869. https://doi.org/10.1155/2011/156869

Pak, M., et al. (2023). Cell-type deconvolution of the Allen Human Brain Atlas: Mapping neuronal and glial contributions to regional gene expression. *Nature Neuroscience, 26*(7), 1055–1067. https://doi.org/10.1038/s41593-023-01318-9

Pourmajidian, M., et al. (2025). Gene expression–derived metabolic maps of the human brain. *bioRxiv*. https://doi.org/10.1101/2025.07.08.663490

Ribeiro, P. F. M., Ventura-Antunes, L., Gabi, M., et al. (2013). The human cerebral cortex is neither one nor many: Neuronal distribution reveals two quantitatively different zones in the gray matter. *Frontiers in Neuroanatomy, 7*, 28. https://doi.org/10.3389/fnana.2013.00028

Schrader, S., Westhoff, A., Piastra, M. C., et al. (2021). DUNEuro: A software toolbox for forward modeling in bioelectromagnetism. *PLoS ONE, 16*(6), e0252431. https://doi.org/10.1371/journal.pone.0252431

Tadel, F., Baillet, S., Mosher, J. C., Pantazis, D., & Leahy, R. M. (2011). Brainstorm: A user-friendly application for MEG/EEG analysis. *Computational Intelligence and Neuroscience, 2011*, 879716. https://doi.org/10.1155/2011/879716

Tran, A. P., Yan, S., & Fang, Q. (2020). Improving model-based functional near-infrared spectroscopy analysis using mesh-based anatomical and light-transport models. *Neurophotonics, 7*(1), 015008. https://doi.org/10.1117/1.NPh.7.1.015008

Vaishnavi, S. N., Vlassenko, A. G., Rundle, M. M., Snyder, A. Z., Mintun, M. A., & Raichle, M. E. (2010). Regional aerobic glycolysis in the human brain. *Proceedings of the National Academy of Sciences, 107*(41), 17757–17762. https://doi.org/10.1073/pnas.1010459107

Zhu, X.-H., Qiao, H., Du, F., et al. (2012). Quantitative imaging of energy expenditure in human brain. *NeuroImage, 60*(4), 2107–2117. https://doi.org/10.1016/j.neuroimage.2012.02.013